IEEE Photonics Journal
An IEEE Photonics Society Publication

Generation of a Train of Ultrashort Pulses Near-Infrared Regime in a Tapered Photonic Crystal Fiber Using Raised-Cosine Pulses

Volume 4, Number 5, October 2012

Samuel Olupitan
K. Senthilnathan
P. Ramesh Babu
Sumeet S. Aphale
K. Nakkeeran

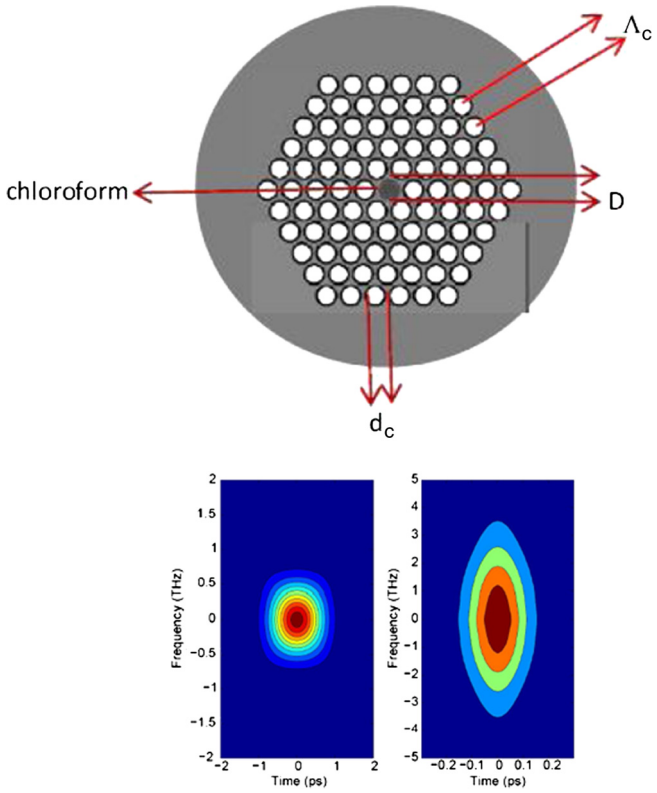

DOI: 10.1109/JPHOT.2012.2208622
1943-0655/$31.00 ©2012 IEEE

Generation of a Train of Ultrashort Pulses Near-Infrared Regime in a Tapered Photonic Crystal Fiber Using Raised-Cosine Pulses

Samuel Olupitan,[1] K. Senthilnathan,[2] P. Ramesh Babu,[2] Sumeet S. Aphale,[1] and K. Nakkeeran[1]

[1]School of Engineering, Fraser Noble Building, King's College, University of Aberdeen, AB24 3UE Aberdeen, U.K.
[2]Photonics Division, School of Advanced Sciences, VIT University, Vellore 632 014, India

DOI: 10.1109/JPHOT.2012.2208622
1943-0655/$31.00 ©2012 IEEE

Manuscript received May 22, 2012; revised July 6, 2012; accepted July 8, 2012. Date of publication July 18, 2012; date of current version August 3, 2012. KSN acknowledges DST, Government of India, for the financial support through the project. Corresponding author: K. Senthilnathan (e-mail: senthee@gmail.com).

Abstract: We consider an optical pulse propagating in a tapered photonic crystal fiber (PCF) wherein dispersion as well as nonlinearity varies along the propagation direction. The generalized nonlinear Schrödinger equation aptly models the pulse propagation in such a PCF. The design of the tapered PCF is based on the analytical results, which demand that the dispersion decrease exponentially and the nonlinearity increase exponentially. In this paper, we adopt the generalized projection operator method for deriving the pulse-parameter equations of the Lagrangian variation method and the collective variable method. Besides, we consider another pulse profile called raised cosine (RC), which is aimed at replacing the conventional hyperbolic secant pulse. From the detailed results, we infer that the initial RC pulse evolves into a hyperbolic secant pulse. Further, in order to minimize the input power requirement, we employ the idea of replacing the solid core in the PCF with chloroform. In addition to the single pulse compression, we also investigate the possibility of multisoliton pulse compression. Here, we consider eight chirped hyperbolic secant pulses as input and generate a train of ultrashort pulses at 850 nm based on the chirped multisoliton pulse compression. In a similar way, we extend this pulse compression with eight RC pulses.

Index Terms: Photonic bandgap, photonic crystal fiber, pulse compression, soliton, ultrashort pulse.

1. Introduction

In recent times, ultrashort pulses (USPs) at shorter wavelengths extending down to the visible region with a high repetition frequency range (GHz–THz) have found wide applications, especially, in bio-photonic sensors [1], optical coherence tomography [2]–[6], materials processing [7], etc. There are some desirable features that USPs need to satisfy, such as being pedestal-free, hyperbolic secant profiled, and transform-limited, for their deployment both in communication and noncommunication-based applications. But, it is very difficult to meet these desirable characteristics even with the carefully configured mode-locked lasers.

Hence, pulse-compression techniques have been the ultimate solution for generating USPs. Of various schemes, the higher order soliton compression and adiabatic pulse compression techniques are the ones in vogue for generating USPs [8]. Although the higher order soliton compression technique provides a large degree of compression, the compressed pulses suffer from

significant pedestals leading to nonlinear interactions between neighboring solitons. On the other hand, adiabatic soliton compression typically demands a monotonically decreasing dispersion profile along the propagation direction [8]. Here, the dispersion varies slowly enough so that the soliton self-adjusts to maintain the balance between dispersion and nonlinearity. Such a compression has already been demonstrated experimentally through a myriad of schemes [8]. Besides, Moores pointed out that an exact chirped soliton solution to the nonlinear Schrödinger (NLS) equation exists when we have exponentially varying dispersion [9]. One of the advantages of the compression scheme based on exponentially varying dispersion is that the condition for adiabatic compression does not need to be satisfied, and therefore, rapid compression is possible. More recently, a technique known as self-similar analysis has been employed to study the linearly chirped pulses in optical fibers [10], [11], fiber Bragg gratings (FBGs) [12], and photonic crystal fibers (PCFs) [13], [14].

Very recently, we have investigated the chirped solitary pulses in the PCF, and based on the results, we have proposed a novel design for generating the pedestal-free as well as chirp-free USPs [13], [14]. In order to ensure the quality of the USPs, it is of paramount importance, from the engineering point of view, to examine the dynamics of the pulses at various stages all along the compression process. In this line, it is customary to study the pulse dynamics by deriving the corresponding pulse-parameter equations. Here, we adopt the projection operator method (POM) that facilitates arriving at two different sets of pulse-parameter equations of the Lagrangian variation method (LVM) and the collective variable method (CVM) [15]. The performance of the proposed compressor can be studied with many possible pulse profiles. However, the interest in choosing raised-cosine (RC) pulse is mainly due to the ease of obtaining the same using the well-known Mach–Zehnder modulators [8], [15]. Even though several authors have reported the pulse compression at different wavelength regimes, pulse compression with two different pulse profiles in the near-infrared region with high compression factor and low pedestal energy, to the best of our knowledge, is being thoroughly addressed in this paper for the first time.

Until recently, the method of realizing USPs has been the usual trend of single pulse compression [8]. Literatures clearly show that the single pulse compression has been accomplished using fibers, FBGs as well as PCFs [8]–[14], [16]–[20]. With the exploding Internet traffic day by day, the ways and means for increasing the bandwidth have attracted greater attention. It is known that the pulse's repetition rate does have a direct impact on the bit rate of the communication systems, which, in turn, is related to the bandwidth. Hence, attempts have been made to use a train of USPs derived from a continuous-wave (cw) source. This is quite often referred to as multisoliton pulse compression. Such a train of USPs has already been generated with a cw source both by using fiber and FBGs [19], [20]. Therefore, here we demonstrate the multisoliton pulse compression at 850 nm using a tapered PCF with both hyperbolic secant and RC pulses.

The discussed pulse compression schemes based on solid-core PCF do have the stringent requirement of high peak power in order to initiate the compression process, which is a basic constraint with these compressors. To overcome this barrier, we present an alternative scheme involving filling out the core of the PCF with a suitable liquid of high nonlinear coefficient to enhance the overall nonlinearity of the medium. In this paper, we choose chloroform to meet the high nonlinearity requirement. In a nutshell, in this paper, we discuss the single-soliton as well as multisoliton pulse compression with both the hyperbolic secant and RC profiles in solid-core and chloroform-filled PCFs (CPCFs).

The paper is laid out as follows. In Section 2, we explain the dynamics of the pulse propagation in a tapered PCF using the NLS equation wherein the dispersion and nonlinearity vary along the propagation direction. In Section 3, we employ POM for hyperbolic secant pulse and obtain the two sets of pulse-parameter equations, namely, LVM and CVM, which relate to the *amplitude*, *pulsewidth*, and *chirp* for explaining the dynamics of pulse compression at various length scales. We also carry out the similar dynamical studies for RC pulses. In this case, we analyze an important issue that emerges during the evolution of RC pulse compression, i.e., convergence of RC compressed pulse into hyperbolic secant pulse. In Section 4, we extend the aforementioned studies

for CPCF. Further, we look at the possibility of generating a train of USPs, again, with both secant and RC profiles, in Section 5. The findings of this work are summarized in Section 6.

2. Pulse Propagation in a Tapered PCF

The pulse propagation in a tapered PCF is described by the following modified NLS equation with the varying dispersion and the nonlinear coefficients [10], [13], [14]:

$$\frac{\partial E}{\partial z} + \frac{i\beta_2(z)}{2}\frac{\partial^2 E}{\partial t^2} = i\gamma(z)|E|^2 E + \frac{g(z)}{2}E. \tag{1}$$

Here, E, z, and t represent the slowly varying field envelope, normalized distance, and time, respectively. The parameters $\beta_2(z)$, $\gamma(z)$, and $g(z)$ are the varying dispersion coefficient, varying nonlinear coefficient, and distributed gain/loss, respectively. We assume that the self-similar solution of (1) is given by

$$E(z,t) = \frac{1}{\sqrt{1-\alpha_{20}D(z)}} R\left[\frac{t-T_c}{1-\alpha_{20}D(z)}\right] \exp\left[i\alpha_1(z) + i\frac{\alpha_2(z)}{2}(t-T_c)^2\right] \exp\left(\frac{G(z)}{2}\right). \tag{2}$$

Here, T_c, $D(z)$, and $G(z)$ are the center of the pulse, the cumulative dispersion, and cumulative gain/loss, respectively. The parameters α_1 and α_2 are the constant phase and chirp, respectively. In (2), the functions $D(z)$, $G(z)$, $\alpha_1(z)$, and $\alpha_2(z)$ are defined by

$$D(z) = \int_0^z \beta_2(z')\,dz' \quad G(z) = \int_0^z g(z')\,dz'$$

$$\alpha_1(z) = \alpha_{10} - \frac{\lambda}{2}\int_0^z \frac{\beta_2(z')\,dz'}{(1-\alpha_{20}D(z'))^2} \quad \alpha_2(z) = \frac{\alpha_{20}}{1-\alpha_{20}D(z)}.$$

Here, λ, α_{10}, and α_{20} are the constants of integration. In order to design an efficient optical pulse compressor, we investigate the generation of chirped bright soliton. The chirped bright soliton formation demands the following necessary and sufficient condition connected to dispersion, nonlinearity, and gain of the medium

$$g(z) = \frac{1}{\rho(z)}\frac{d\rho(z)}{dz} + \frac{2\alpha_{20}\beta_2(z)}{1-\alpha_{20}D(z)} \tag{3}$$

where $\rho(z) = \beta_2(z)/\gamma(z)$. Finally, the chirped bright solitary wave in a tapered PCF is given by

$$E(z,t) = \sqrt{\frac{|\beta_{20}|\exp(-\sigma z)}{\gamma_0\exp(\eta z)}}\frac{1}{T_0\exp(-\sigma z)}\operatorname{sech}\left\{\frac{t-T_c}{T_0\exp(-\sigma z)}\right\} \times \exp\left[i\alpha_{10} + \frac{i\beta_{20}}{2\sigma T_0^2}[1-\exp(\sigma z)] + \frac{i\sigma\exp(\sigma z)}{2\beta_{20}}(t-T_c)^2\right] \tag{4}$$

where T_0 and α_{20} are the initial pulsewidth parameter and initial chirp, respectively. Equation (4) represents the bright soliton for varying profiles of the medium, namely, $\beta_2(z)$, $\gamma(z)$, and $g(z)$. It should be noted that there exists a physical constraint that dictates that not all the three distributed parameters can be varied simultaneously. However, two of them can be varied by keeping the third one a constant. Therefore, we consider a most physically valid system wherein the dispersion and nonlinearity vary along the propagation direction with the loss remaining a constant. On this line, the dispersion and nonlinearity vary in the following way:

$$\beta_2(z) = \beta_{20}\exp(-\sigma z), \quad \gamma(z) = \gamma_0\exp(\eta z).$$

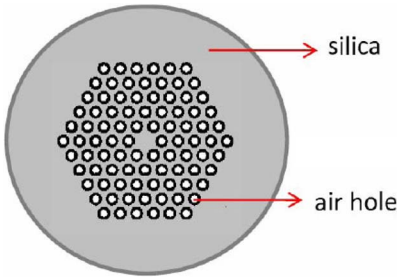

Fig. 1. Design of a tapered PCF [13].

Here, the parameters β_{20} and γ_0 are initial dispersion and nonlinearity of the medium, respectively. Further, σ is the decay rate of the dispersion, and η is the growth rate of the nonlinearity. Now, in order to prove that the loss parameter is a constant one, we substitute the dispersion and nonlinearity varying parameters in (3) and obtain the following expression for $g(z)$

$$g(z) = -\eta - \frac{\sigma(\nu - 1)}{\nu - 1 + \exp(-\sigma z)} \tag{5}$$

where

$$\nu = \frac{\sigma}{\alpha_{20}\beta_{20}}. \tag{6}$$

The loss/gain profile becomes a constant only when $\nu = 1$. This implies that $g(z) = -\eta$. Thus, the hitherto mentioned analytical result, i.e., (4) is valid only when the dispersion decreases exponentially and the nonlinearity increases exponentially with the loss remaining as a constant. These are the crucial conditions that are to be met for the formation of the chirped optical soliton.

Interestingly, the condition $g(z) = -\eta$ drives the loss coefficient same as the exponential growth rate of the nonlinearity. One can implement the variable transformation for the electric field envelope, $E = E'\exp\left[\left(-\frac{\eta}{2}\right)z\right]$ in (1). The resulting NLS equation in terms of E' will have no loss term, and the nonlinear coefficient $\gamma(z)$ will become a constant. However, we are not interested in that kind of PCF for pulse compression at near-infrared regime. Instead, we desire to have the condition on the loss coefficient as $g(z) = -\eta$ and proceed further for an appropriate design of PCF to help generate USPs. Thus, the conditions on dispersion, nonlinearity, and loss play an indispensable role in designing the PCF for the construction of an efficient pulse compressor. In the tapered PCF, size of the air hole must vary exponentially to meet these required conditions. Hence, the ratio d/Λ varies exponentially from 0.6 to 0.59. Here, d is the diameter of the hole, and Λ is the pitch. Further, the pitch, Λ, varies from 1 to 0.95 μm. While choosing PCF parameters for designing tapered PCF, it should be remembered that the dispersion decreases from the maximum possible value to the minimum value within single-mode regime. Since the path of air hole size variation is exponential, one can achieve dispersion-decreasing and nonlinearity-increasing PCF, as shown in Fig. 1.

3. Pulse Compression in a Solid Core PCF

3.1. USPs With Hyperbolic Secant Profile

To illustrate the effect of pulse compression based on the analytical results, we consider a PCF of length $L = 4L_D$, where the dispersion length, $L_D = T_0^2/\beta_2$. We calculate the group velocity dispersion (GVD) of the PCF through the finite-element method (FEM), and its value at 850 nm has been found to be 27.24 ps/nm/km. The nonlinear coefficient of silica is 2.3×10^{-20} m^{2}W^{-1}.

Since the calculated linear length is 19.72 m for a given input pulsewidth (FWHM) of 800 fs, the compression can be obtained at a shorter length compared with the case of conventional fiber.

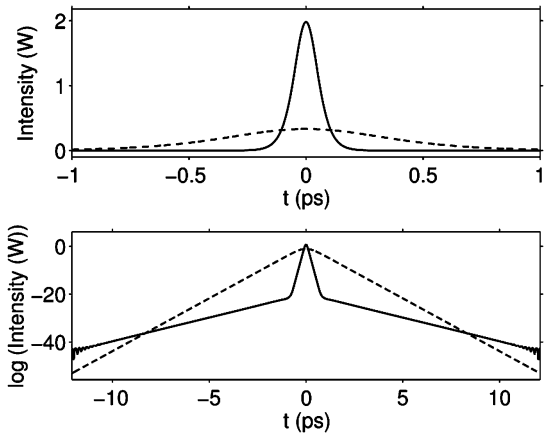

Fig. 2. Intensity profiles of initial (dashed lines) and compressed output pulse (solid lines) of a chirped solitary pulse. The physical parameters are $\alpha_{20}/2\pi = -0.092$ GHz/ps, $\beta_{20} = 27.24$ ps/km/nm, $\sigma = 0.0121$, $\gamma_0 = 0.1519$ W^{-1}m^{-1}, and $\eta = 0.0008$.

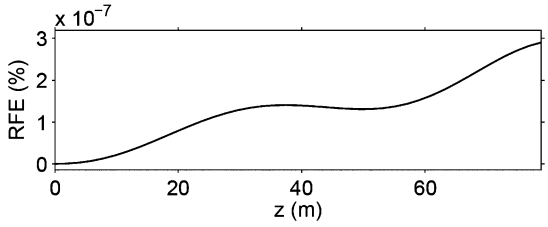

Fig. 3. RFE evolution during the self-similar pulse compression process.

Using FEM, GVD at the end of the PCF is found be 10.571 ps/nm/km. From the computed dispersion and nonlinear data by FEM, we determine the dispersion decay rate σ as 0.0121 and nonlinearity growth rate η as 0.0008 by means of curve fitting. In (6), when $\nu = 1$, we get $\sigma = \alpha_{20}\beta_{20}$, and hence, the initial chirp is calculated as $\alpha_{20}/(2\pi) = -0.092$ GHz/ps. Fig. 2 demonstrates the compression of a chirped solitary pulse wherein the dotted and solid lines represent the intensity profiles of initial and final compressed pulses, respectively. From the logarithmic plot shown at the bottom of Fig. 2, it is obvious that the compressed pulse possesses a negligible amount of pedestals that practically are hardly worrisome. We determine this pedestal energy in terms of residual-field energy (RFE) with the following expression:

$$\mathrm{RFE}(\%) = \frac{\int_{-\infty}^{\infty} |E - E_1|^2 \, dt}{\int_{-\infty}^{\infty} |E|^2 \, dt} \times 100$$

where E is the electric field envelope calculated by solving the NLS equation using the split-step Fourier method, and E_1 is the best fit of the hyperbolic secant pulse obtained by least-mean-square fit for all the six parameters (amplitude, pulse peak temporal position, pulsewidth, chirp, velocity, and constant phase).

This pedestal energy calculation here is exactly the same as that of the RFE calculation carried out in the collective variable theory [21]. While the Newton–Raphson method is used to find the best-fit ansatz function parameters as in [21], in this work, we adopt the least-mean-square method. Fig. 3 depicts the pedestal energy evolution during the self-similar pulse compression process. Further, this figure confirms that the pedestal energy generated during the compression process is

highly negligible on account of the fact that it is only a fraction of attojoule $(10^{-18}$ J$)$. Hence, based on this analysis, we infer that one can generate clean short pulses that do not interact with the neighboring pulses unlike the case of short pulses obtained from conventional compressors. By this method, the compression factor is calculated to be 2.6.

In addition, we derive the pulse-parameter equations for further analyzing the evolution of the compressed pulses in terms of the associated parameters, namely, amplitude, pulsewidth, and chirp. Here, we adopt POM that facilitates arriving at two different sets of pulse-parameter equations of LVM and CVM. As the self-similar analysis reveals the wave shape of the bright solitary pulse as hyperbolic secant, we use the following hyperbolic secant function as an ansatz to derive the pulse-parameter evolution equations

$$E = x_1 \operatorname{sech}\left(\frac{t}{x_2}\right) \exp\left(i\frac{x_3}{2}t^2 + ix_4\right) \tag{7}$$

where x_1, x_2, x_3, and x_4 represent the pulse amplitude, width, chirp, and phase, respectively. Using this ansatz in the modified NLS equation, we end up with two sets of pulse-parameter equations. However, both sets of equations are of same functional forms, differing only in their corresponding coefficients. The functional forms for both the methods are given by,

$$\begin{aligned}
\frac{dx_1}{dz} &= \frac{\beta_2(z)}{2} x_1 x_3 \\
\frac{dx_2}{dz} &= -\beta_2(z) x_2 x_3 \\
\frac{dx_3}{dz} &= \beta_2(z)\left(x_3^2 - \frac{\delta_1}{x_2^4}\right) - \frac{\delta_2 \gamma(z) x_1^2}{x_2^2} \\
\frac{dx_4}{dz} &= \frac{\delta_3 \beta_2(z)}{x_2^2} + \delta_4 \gamma(z) x_1^2.
\end{aligned} \tag{8}$$

Here, the constants δ_n's ($n = 1$ to 4) are different. For LVM, the δ_n's are given by

$$\delta_1 = \frac{4}{\pi^2} \quad \delta_2 = \frac{4}{\pi^2} \quad \delta_3 = \frac{1}{3} \quad \delta_4 = \frac{5}{6}.$$

On the other hand, the constants δ_n's for CVM are given by

$$\delta_1 = \frac{30}{\pi^4} \quad \delta_2 = \frac{30}{\pi^4} \quad \delta_3 = \frac{1}{6} + \frac{5}{4\pi^2} \quad \delta_4 = \frac{2}{3} + \frac{5}{4\pi^2}.$$

These pulse-parameter equations, indeed, do very clearly explain the behavior of the compressed self-similar pulses in different length scales of the PCF structure.

To explore into the dynamics of the pedestal-free USPs, we solve the two sets of pulse-parameter equations numerically. Fig. 3 (a1, b1, and c1) illustrates the evolution of the pulse amplitude, width, and chirp, having been examined using LVM's equations of motion. To confirm these results further, we solve the modified NLS equation using the split-step Fourier method.

Here, the solid curve corresponds to the analytical results, dot-dashed to numerical results, and dotted ones to LVM. Similarly, for CVM, the corresponding evolution plots are designated as a2, b2, and c2. From Fig. 3 (a1, b1 and a2, b2), the intensity of the pulse under compression increases exponentially at different length scales, and the corresponding pulsewidth decreases exponentially. This process further confirms the rapid compression. During the compression process, the chirp associated with the compressed pulses increases exponentially over the distance, and the same is clearly depicted in Fig. 4 (c1 and c2). Thus, the dechirper is required in the proposed compressor scheme. It may be noted that the variations of amplitude, pulsewidth, and chirp with respect to the distance are all exactly one and the same when studied analytically, semianalytically (both LVM and CVM) as well as numerically, as evident from Fig. 4.

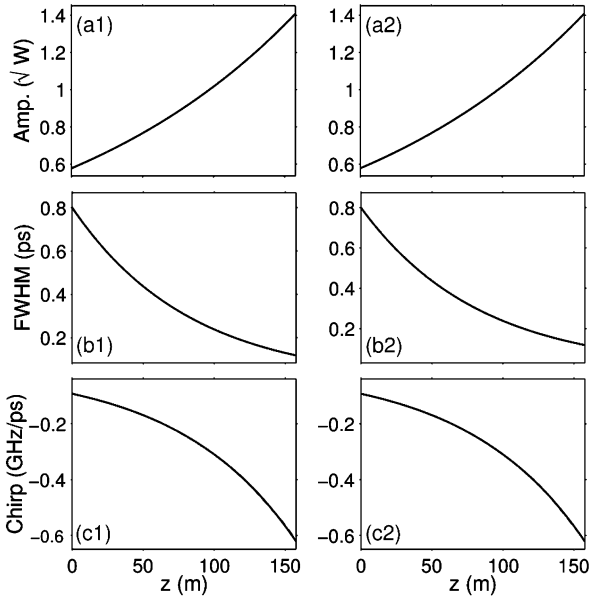

Fig. 4. Comparison of hyperbolic secant pulse evolution changes in terms of amplitude, pulsewidth, and chirp for LVM (a1, b1, c1) and CVM (a2, b2, c2). The physical parameters are same as in Fig. 2.

3.2. USPs Using RC Profile

In practice, the generation of pulses of hyperbolic secant profile is difficult at high bit rates. But Mach–Zehnder modulators, which form an important entity of optoelectronic communication systems, do provide RC pulses, which, in turn, could serve as a better alternative for generating USPs. More detailed study on the dynamics of RC ansatz pulse propagation in dispersion-managed fiber systems has already been reported [22]. The RC ansatz is written as

$$E = \frac{x_1}{2}\left[1 + \cos\left(\frac{\pi t}{x_2}\right)\right]\exp\left(\frac{ix_3 t^2}{2} + ix_4\right). \tag{9}$$

Now, we carry out the pulse compression studies for the RC pulse too. In this line, we once again solve the governing NLS equation with hitherto mentioned RC ansatz as an initial condition. It is to be noted that the investigations on RC pulse have been carried out with the same physical parameters that were employed in the case of hyperbolic secant pulses. It is practically difficult to match the energy, peak amplitude, and pulsewidth simultaneously for a hyperbolic secant pulse and an RC pulse. Hence, we match only peak amplitude and energy of both the profiles. Eventually, the third parameter, namely, pulsewidth, can be calculated from the expressions relating to the energy of RC and hyperbolic secant pulse profiles. We delineate the compression results by means of spectrograms as well as intensity plots with linear and logarithmic scales.

Fig. 5 depicts the spectrogram for initial and compressed pulses of RC profile. From the figure, it is clear that the spectrogram of compressed RC pulse has relatively smaller pulsewidth with corresponding expansion in the spectral domain. Fig. 6 sheds light on the compression of chirped RC pulse in terms of intensity plots. The dotted and solid lines represent the initial and final compressed pulses, respectively. From the logarithmic plot in Fig. 6, it can be seen that the compressed RC pulse exhibits only a negligible amount of pedestals.

We compute the amount of pedestal generated in the same way as in the previous section. The pedestal energy evolution of an RC pulse is shown in Fig. 7.

An important worthy point to be noted is that the amount of pedestal energy generated is just only half the amount of pedestal energy produced by hyperbolic secant pulse in the adiabatic pulse compression technique, which has been discussed in [13]. Thus, in the self-similar pulse

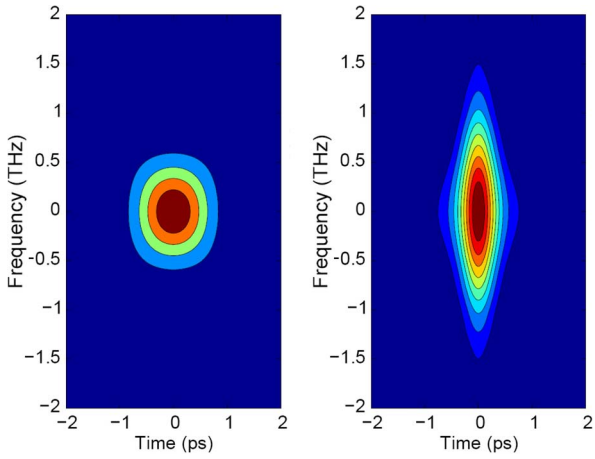

Fig. 5. Spectrogram (left) of initial pulse of 800 fs FWHM pulsewidth with an initial peak intensity 0.33 W. Spectrogram (right) of final compressed pulse produced by self-similar process after a length of $4L_D$. The physical parameters are same as in Fig. 2.

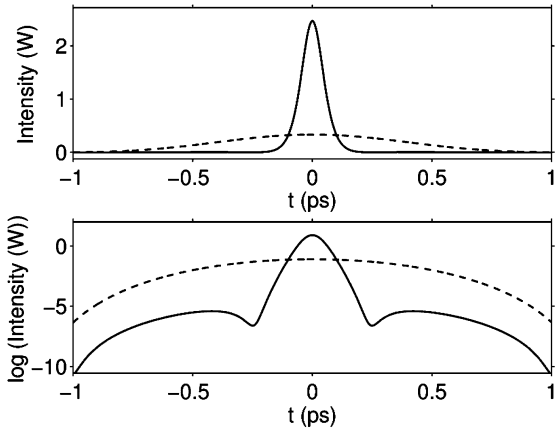

Fig. 6. Compression of a chirped RC pulse for the same parameter values as in Fig. 2.

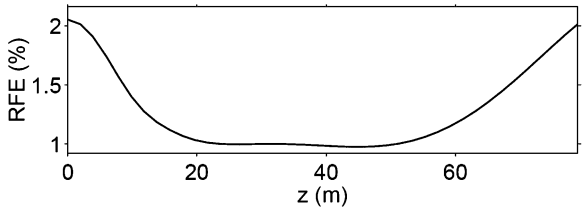

Fig. 7. RFE evolution of an RC pulse for the same parameter values as in Fig. 2.

compression scheme, the advantage of deploying the RC profiles for the pulse compression stems from the compromising level of pedestals compared with that of hyperbolic secant pulses. However, RC compression scheme with self-similar analysis is superior to adiabatic compression using hyperbolic secant pulse. Hence, we believe that the compressed RC pulses obtained through self-similar analysis will find applications that require USPs.

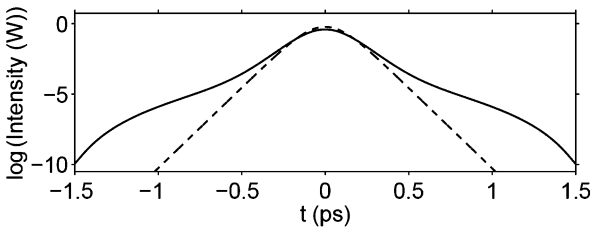

Fig. 8. Comparison of a chirped RC compressed pulse with that of hyperbolic secant pulse in logarithmic scale for the same parameter values as in Fig. 2.

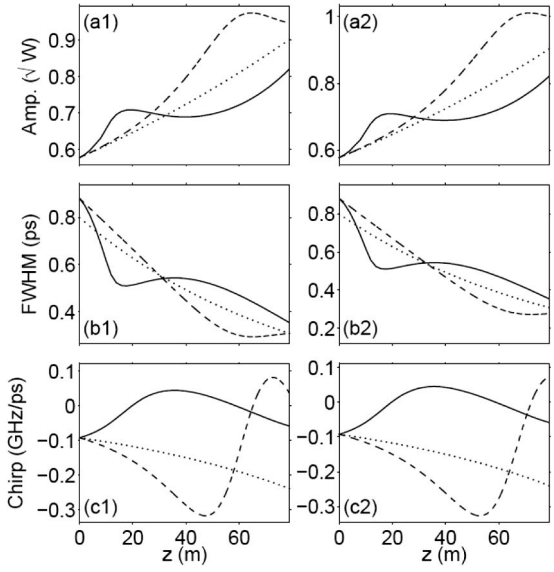

Fig. 9. Amplitude, pulsewidth, and chirp evolutions over $4L_D$ distance propagation. In Figs. (a1), (b1), and (c1) and (a2), (b2), and (c2), the dashed lines represent the results of LVM and CVM, respectively. The solid and dotted lines correspond to full numerical and analytical results, respectively.

3.3. Convergence of Compressed RC Pulse

As we study the compression of RC pulse profile, it is better to analyze the nature of the profile at the end of the compression process. Therefore, we fit the final compressed RC pulse profile with the hyperbolic secant pulse profile. In Fig. 8, while the solid curve represents the compressed RC pulse, the dotted one belongs to the hyperbolic secant pulse. From the logarithmic plot, we infer that the compressed RC pulse tries to converge into the hyperbolic secant profile, which is reflected from its tendency to coalesce into hyperbolic profile. Thus, the initial RC pulse profile evolves into a hyperbolic secant pulse profile during the compression process.

Having discussed the RC pulse compression by means of complete numerical simulation, next, we would like to analyze how these numerical results would evolve when compared with variational equations, i.e., pulse-parameter equations of hyperbolic secant ansatz. Henceforth, we compare the numerical results of RC compressed pulses with that of variational equations of hyperbolic secant. The evolutions of RC pulse parameters are shown in Fig. 9 wherein (a1, b1, and c1) and (a2, b2, and c2) correspond to the LVM and CVM results, respectively. From the results, it is obvious that the amplitude and pulsewidth parameters calculated from the numerical analysis are oscillating closely over the respective self-similar analytical solution parameters. However, in contrast to analytical results, interestingly, the chirp associated with the RC compressed pulse almost attains zero as shown in Fig. 9 (c1 and c2).

In the case of RC pulse compression, the chirp evolves in such a way to compensate for the initial value of the chirp. We find that the chirp oscillates around the zero value. Thus, the compressed RC

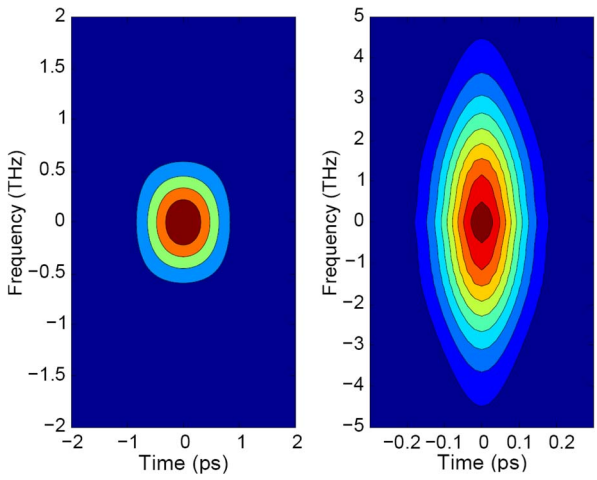

Fig. 10. Spectrogram (left) of initial RC pulse. Spectrogram (right) of final compressed pulse over a distance of $8L_D$. The physical parameters are same as in Fig. 2.

pulse does not require the dechirper, and this is one of the primary advantages of deploying RC profile for the pulse compression.

From the results of Figs. 8 and 9, we can conclude that the initial RC pulse slowly evolves into hyperbolic secant profile, as hyperbolic secant pulse is the exact solution of the system as per the self-similar analysis. Thus, RC can serve as a better alternative for hyperbolic secant pulse in generating the USPs if one could compromise with the tiny amount of pedestal energy generated by RC pulse.

It turns out to be a fundamental curiosity to investigate on the evolution of the RC compressed pulses in the compression process extending beyond $4L_D$. Upon propagating the RC pulse beyond $4L_D$, we expect a much pronounced convergence of the final compressed RC pulse closer to the hyperbolic secant profile. In this line, we carry out the RC pulse compression simulation over a distance of $8L_D$. Fig. 10 shows the spectrograms of the initial pulse as well as the compressed RC pulse after propagating over a distance of $8L_D$. The spectrogram of the compressed RC pulse for a propagation distance of $8L_D$ is relatively more elliptical compared with that of the one of $4L_D$. The higher degree of ellipticity in the case of $8L_D$, which is also the case for compressed hyperbolic secant profile, substantiates our argument that RC compressed pulse turns into hyperbolic secant profile. Small oscillations in the contour lines of the spectrogram of the compressed pulse show the existence of tiny pedestals.

The convergence of RC compressed pulse can also be understood by comparing the intensity plots of both RC and hyperbolic secant pulses. When compared with Fig. 8 obtained for $4L_D$, we find that a major portion of the compressed RC pulse does exactly match with the hyperbolic pulse in Fig. 11, which is plotted for $8L_D$. For further confirming the convergence of RC compressed pulse, we once again analyze the evolutions over a distance of $8L_D$ by numerically solving the pulse-parameter equations of both LVM and CVM, and the relevant results are presented in Fig. 12. From Fig. 12, the amplitude and pulsewidth parameters calculated from numerical analysis oscillate closely over the respective self-similar analytical results. An important point to be noted here is that the amplitude of these oscillations gets reduced as the pulse propagates for a longer distance, suggesting that they are converging toward the exact self-similar hyperbolic secant pulse.

Also, the chirp evolution for $8L_D$ distance of propagation clearly shows that the initial chirp is almost compensated. Thus, we infer that the chirp almost attains zero value for longer distance of propagation. With all these findings, we claim that the proposed PCF pulse compressor based on self-similar analysis not only produces high-quality compressed pulses but also works like a pulse shape modulator since it has the potential to compress any pulse profiles in addition to hyperbolic secant pulse. Another merit of the proposed compressor lies in its ability to work with pulses of any

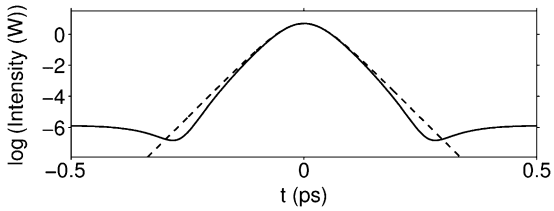

Fig. 11. Comparison of a chirped RC compressed pulse with that of hyperbolic secant pulse in logarithmic scale for the same parameter values (as in Fig. 2) for $8L_D$ propagation distance.

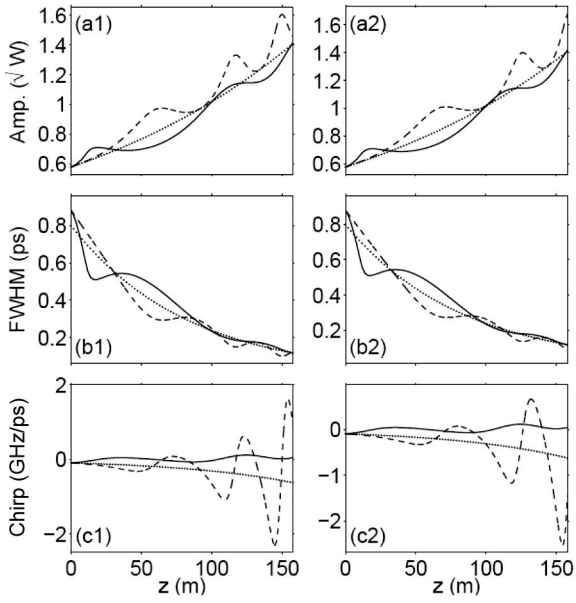

Fig. 12. Amplitude, pulsewidth, and chirp evolutions over $8L_D$ distance propagation. In Figs. (a1), (b1), and (c1) and (a2), (b2), and (c2), the dashed lines represent the results of LVM and CVM, respectively. The solid and dotted lines correspond to full numerical and analytical results, respectively.

profiles matching to the case of slightly perturbed hyperbolic secant profile such that the input profile evolves as hyperbolic secant profile upon compression.

4. RC Pulse Compression in a CPCF

In the previous sections, we have discussed the feasibility of achieving pulse compression within a short distance when compared with conventional fiber. Nonetheless, the process requires huge amount of peak power for inducing required nonlinearity to cope with the enhanced dispersion in PCF. In this section, we try to overcome this power requirement by filling out the core of the PCF with a suitable liquid possessing the desired nonlinear coefficient that would be sufficient enough for the pulse compression with a relatively less input power. Very recently, studies on supercontinuum generation [23] and pedestal-free USPs in terms of soliton-type pulses have been carried out in CPCF [13].

The proposed CPCF is shown in Fig. 13(b). The filling of chloroform can be done in the core of the PCF by capillary force technique [24]. This CPCF has $d_c/\Lambda_c = 0.8$, with $\Lambda_c = 1$ μm. Here, the core diameter D is chosen to be the same as the diameter of air hole in the outer ring d_c, i.e., $D = d_c$. In order to meet with the requirement of exponentially dispersion-decreasing profile and exponentially nonlinearity-increasing profile, we design the tapered CPCF by varying the size of the air hole from 0.8 to 0.665 and pitch from 1 μm to 1.08 μm [6]. By FEM, we calculate the GVD to be

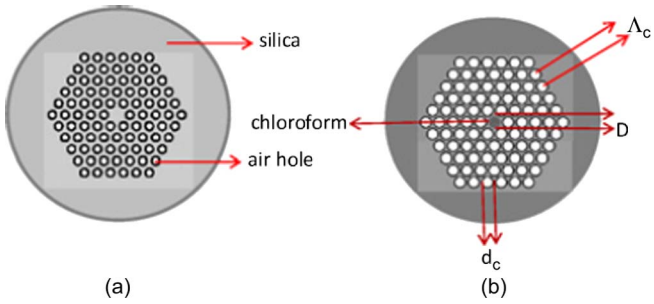

Fig. 13. (a) Schematic diagram of a solid-core PCF and a (b) CPCF [13].

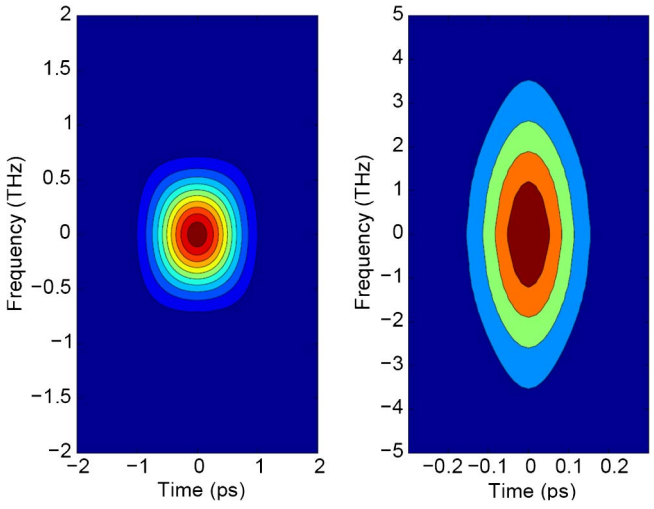

Fig. 14. Spectrogram (left) of initial RC pulse. Spectrogram (right) of final compressed pulse over a distance of $8L_D$ in CPCF. The physical parameters are $\alpha_{20}/2\pi = -0.092$ GHz/ps, $\beta_{20} = 68.72$ ps/km/nm, $\sigma = 0.03$, $\gamma_0 = 26.3$ W^{-1}m^{-1}, and $\eta = 0.006$.

68.71 ps/nm/km at 850 nm. This is 2.5 times greater than the GVD value of the solid-core PCF, which is 27.24 ps/nm/km. Further, the nonlinearity of CPCF is almost 200 times greater than that of the solid-core PCF. Therefore, by using CPCF, one can achieve the same compression factor with the input power being 200 times lower than the requirement for the solid-core PCF. Fig. 14 includes the spectrogram of the initial pulse as well as the compressed one at $8L_D$. It may be noted that the spectrogram of compressed RC pulse being highly elliptical signifies the crucial point that RC pulse evolves into hyperbolic secant profile upon being compressed. Further, small oscillations in the contour lines in the spectrogram of the compressed pulse get vanished unlike the case of the solid-core PCF.

Comparing the intensity profiles of hyperbolic secant as well as RC pulse both in the case of solid-core PCF (as in Fig. 11) and the proposed CPCF (as in Fig. 15), one could easily figure out that the matching between the profiles of hyperbolic secant and RC pulse is more conspicuous in the case of CPCF only.

As discussed previously, we now delve into the dynamics of the RC pulse compression in CPCF. The discussions relating to the variation in amplitude, pulsewidth, and chirp with respect to propagation distance are almost same here too. However, an important point to be highlighted here is that the amplitude of oscillations is much lower when compared with the solid-core PCF. This advantage stems from filling out the appropriate liquid within the core to augment to the nonlinearity (see Fig. 16).

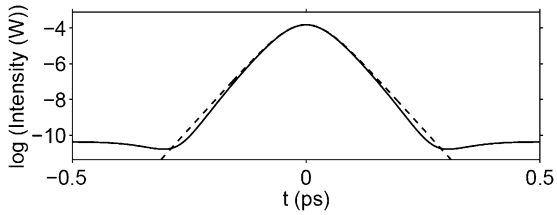

Fig. 15. Comparison of a chirped RC compressed pulse with that of hyperbolic secant pulse in logarithmic scale for the same parameter values as in Fig. 14 for $8L_D$ in CPCF.

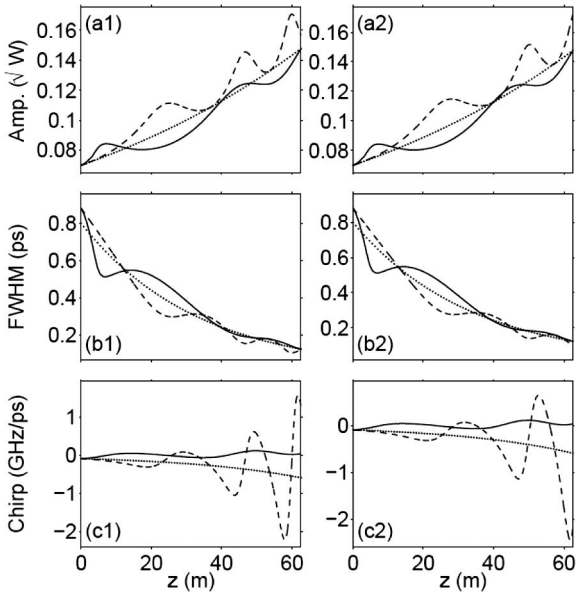

Fig. 16. Amplitude, pulsewidth, and chirp evolutions over $8L_D$ distance propagation in CPCF. In Figs. (a1), (b1), and (c1) and (a2), (b2), and (c2), the dashed lines represent the results of LVM and CVM, respectively. The solid and dotted lines correspond to full numerical and analytical results, respectively.

Thus far, we have investigated the compression of RC pulse in PCF and CPCF, designed using self-similar analysis. We find that the RC-shaped pulse can undergo the same amount of compression like the hyperbolic secant pulse, but with generation of tiny pedestals. The amount of pedestal generated is quantified in terms of pedestal energy, which is calculated by the difference in the electric field envelopes between the RC compressed pulse and the best-fit hyperbolic secant pulse whose parameters are the same as that of the RC pulse. We observe that during the compression of the RC pulse, the profile of the pulse slowly evolves toward the hyperbolic secant shape as per self-similar analysis. More importantly, initial chirp of the RC pulse gets compensated during compression in both PCF and CPCF compressors, which, in-turn, can avoid the need for the dechirper in the proposed self-similar-analysis-based PCF compressors. From all the results reported here for the RC pulse compression, we conclude that the CPCF compressor is a better device to efficiently compress pulses with initial profile, different from that of the hyperbolic secant shape.

5. Multi-Pulse Compression in PCF and CPCF

5.1. Generation of a Train of USPS With Hyperbolic Secant Pulses

Based on the results presented in Sections 2–4, one can understand that the proposed compressor effectively generates the short pulse when input is a single broad pulse in time domain.

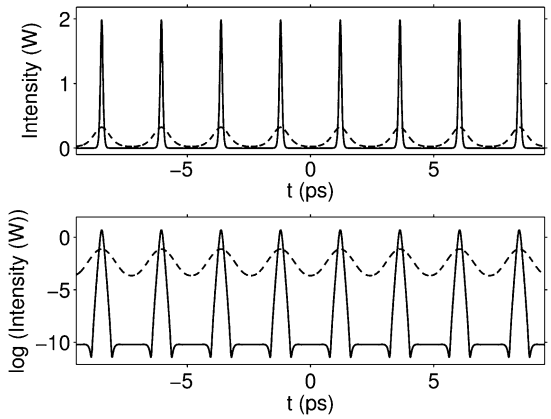

Fig. 17. Compression of a train of chirped solitary pulses in solid-core PCF over a propagation distance of $8L_D$. Dashed and solid lines represent the intensity plots of initial and compressed pulse trains, respectively. The parameter values are same as in Fig. 2.

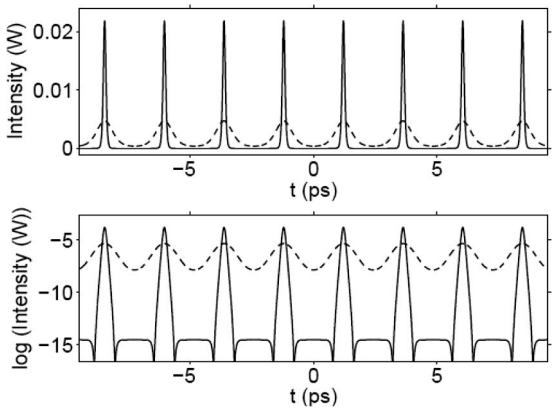

Fig. 18. Compression of a train of chirped solitary pulses in CPCF over a propagation distance of $8L_D$. Dashed and solid lines represent the intensity plots of initial and compressed pulse trains, respectively. The parameter values are same as in Fig. 14.

In this section, the objective is to check if the proposed compressor could generate a train of short pulses with the input being more than one pulse. For the illustration purpose, we take eight chirped hyperbolic secant pulses for generating a train of USPs at 850 nm by means of the chirped multisoliton pulse compression.

Fig. 17 demonstrates the compression of chirped multisolitary pulses, wherein the dotted and solid lines represent the intensity profiles of initial and final compressed pulses, respectively. Here, the initial pulsewidth of 800 fs, measured as FWHM, is compressed to 200 fs over a propagation distance of $8L_D$. In this paper, the separation between hyperbolic secant pulses is chosen to be the same as that of RC pulses. From the logarithmic plot shown at the bottom of Fig. 17, it is obvious that the compressed pulses exhibit the negligible amount of pedestals. These pedestals arise because of the nonlinear tail interactions between pulses. Further, the initial pulse train possesses a very high degree of interacting electric fields in the tail parts, and the same is quite evident from the logarithmic intensity plot.

As has been delved in the single pulse compression, for multisoliton pulse compression too, we carry out the compression studies in the CPCF for reducing the required peak power. A train of short pulses with the minimum peak power obtained from the temporally broadened hyperbolic pulses is shown in Fig. 18. The impact of filling chloroform in the core of the PCF can very well be

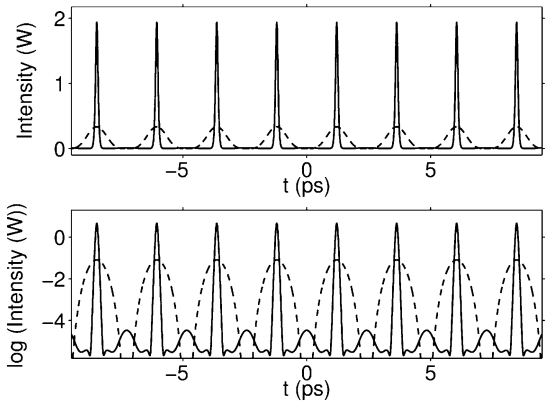

Fig. 19. Compression of a train of RC pulses in solid-core PCF over a propagation distance of $8L_D$. Dashed and solid lines represent the intensity plots of initial and compressed pulse trains, respectively. The parameter values are same as in Fig. 2.

appreciated by the awful decrement in the peak power of the compressed pulses from CPCF as against the case of solid-core PCF. An important point to emphasize at this juncture is that the amount of pedestal produced in the CPCF compression scheme is less than that in the case of the solid-core PCF.

5.2. Generation of a Train of USPS With Chirped RC Pulses

It is important to underpin the deployment of RC pulses in place of hyperbolic secant profiled pulses, without compromising much on the magnitude of the pedestals. In the earlier discussions, we have demonstrated the compression of both hyperbolic secant and RC pulse profiles with the input being a single pulse. From the detailed investigation, it could be inferred that the compressed RC pulse almost attains the zero chirp, whereas the hyperbolic secant pulse is not completely chirp-free. As a result, RC pulses obviate the necessity for a dechirper, and undoubtedly, this results in realizing a compact and efficient pulse compressor. Another important point is that the RC pulse slowly evolves into hyperbolic secant-shaped pulse. These interesting results are the main driving force for investigating a train of USPs using RC pulses against the compressed hyperbolic secant train of pulses.

Fig. 19 demonstrates the compression of chirped RC pulses, wherein the dotted and solid lines represent the intensity profiles of initial and final compressed pulses, respectively. From the logarithmic plot shown at the bottom of Fig. 19, it could be seen that the compressed RC pulses have some pedestals whose magnitude is larger than that of the compressed hyperbolic secant pulses with the same separation between the pulses. These pedestals appear because of nonlinear tail interaction between pulses as well as deviation of the initial RC pulse profile from the self-similar hyperbolic secant pulse. In order to understand the global behavior of the compressed RC pulses, we compare the intensity plot of compressed hyperbolic secant pulses with that of the compressed RC pulses, and the same is depicted in Fig. 20. Here, the solid and the dotted curves relate to the cases of RC and hyperbolic secant pulses, respectively.

From the logarithmic plot, we find that the RC pulse profiles do exactly match with that of the hyperbolic secant pulses. Thus, at the end of the compression process, these initial RC pulses do evolve into hyperbolic secant pulses.

The next natural curiosity is to explore into the compression of RC pulses in the CPCF. Fig. 21 shows the compression of chirped RC pulses, wherein the dashed and solid lines indicate the intensity profiles of initial and final compressed pulses, respectively. From the logarithmic plot, it turns out that the compressed pulses have some pedestals that are greater than the case of compressed hyperbolic secant pulses with the separation between the pulses being the same. As expected, the pedestals generated in the case of CPCF compressor are lesser than the solid-core PCF compressor.

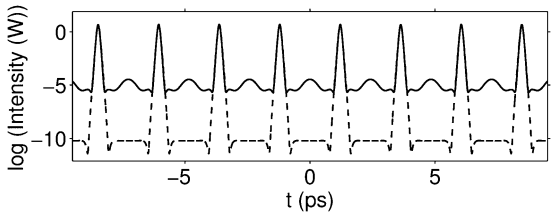

Fig. 20. Comparison of intensity plots of a train of compressed RC pulses with that of hyperbolic secant pulses in logarithmic scale.

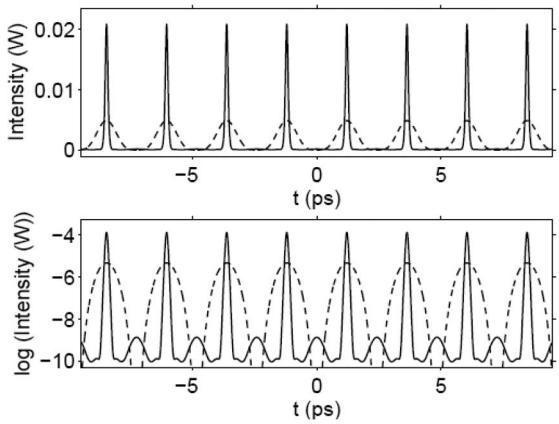

Fig. 21. Compression of a train of RC pulses in CPCF over a propagation distance of $8L_D$. Dashed and solid lines represent the intensity plots of initial and compressed pulse trains, respectively. The parameter values are same as in Fig. 14.

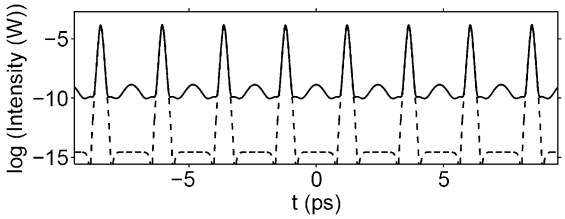

Fig. 22. Comparison of intensity plots of a train of compressed RC pulses with that of hyperbolic secant pulses in logarithmic scale in CPCF.

Fig. 22 illustrates the comparison of the compressed RC pulses (solid lines) with that of compressed hyperbolic pulses (dashed lines) in CPCF. This logarithmic plot throws light on the merit of the RC compressed pulses over the compressed hyperbolic pulses.

It is very interesting to note that the degree of pedestals generated while compressing RC pulses in CPCF is same as the pedestals generated upon compressing hyperbolic secant pulses in solid-core PCF. This crucial aspect leads to relatively a better convergence of compressed RC pulses into hyperbolic secant profile over a propagation distance of $8L_D$ when solid-core PCF is replaced by CPCF.

6. Conclusion

Based on the analytical results of chirped soliton, we have designed a pulse compressor using a tapered PCF and discussed the possibility of generating pedestal-free USPs around 850 nm. A complete dynamics of the compressed pulses, such as the variations in the amplitude, pulsewidth,

and chirp, has also been studied using POM. Hence, we have derived two different sets of pulse-parameter equations of LVM and CVM. We have observed that the analytical, semianalytical, and full numerical results pertaining to amplitude, pulsewidth, and chirp match very well in all the domains of study. It may be noted that the compressed hyperbolic pulses have some residual chirp and hence require a dechirper. On the other hand, compressed RC pulses are almost chirp-free, and this turns out to be a major advantage of RC pulse compression scheme compared with those in vogue. In addition, in order to analyze the performance of the proposed compressor, an attempt has also been made for compressing the RC pulse. We did fit the compressed RC pulse with that of hyperbolic secant pulse. The RC compressed pulse evolution has been studied for $4L_D$ as well as $8L_D$ distance of propagation. From the result, it has been found that the RC pulse has evolved into hyperbolic secant pulse for a propagation distance of $8L_D$.

We have found that the hitherto discussed compressor demands a large input power for initiating the compression process. Thus, in this work, we have also addressed this crucial issue and prescribed the remedy for the same by filling the chloroform liquid in the core region of the PCF. This new design helps enhance all the characteristics of the compressed pulse. Consequently, CPCF turns undoubtedly superior to the conventional solid-core PCF. Thus, the advantage of deploying the RC profiles for the pulse compression stems from the compromising level of pedestals compared with that of hyperbolic secant pulses.

In addition to the issues discussed above, we have also demonstrated the multisoliton pulse compression with the eight hyperbolic secant pulses. But the previous experience clearly indicates that the generation of pulses of hyperbolic secant profile has always been a challenging problem. To overcome this barrier, we have deployed RC pulses as an alternative to the hyperbolic secant profile. In this paper, the separation between hyperbolic secant pulses has been chosen to be the same as that of RC pulses. Here also, we fit the compressed RC pulses with that of hyperbolic secant pulses. From the results, we have found that the compressed RC pulses have evolved into the hyperbolic secant pulses. Thus, it can be seen that, while the train of solitary pulses generated with the input being hyperbolic secant pulses almost have no pedestals, the one produced by the RC pulses does have pedestals, although down to a negligible level. We reiterate that the amount of pedestals generated while compressing RC pulses in CPCF are same as the pedestals generated with the hyperbolic secant pulses in solid-core PCF. This vital point assures a better convergence of compressed RC pulses into hyperbolic secant profile over a propagation distance of $8L_D$ when solid-core PCF is replaced by CPCF.

To sum up the various pulse compression schemes that have been discussed in this work over a distance of $8L_D$, we would like to mention that the pulse compression, both as a single pulse and a train of pulses, has been done with hyperbolic secant as well as RC profiles in solid-core PCF as well as CPCF. Revisiting the various results, we firmly believe that the scheme involving generation of a train of USPs by using CPCF unarguably stands unique among the rest of the schemes owing to its merits discussed in the text.

Acknowledgment

Authors wish to thank S. Sivabalan and R. Vasantha Jayakantha Raja for fruitful discussions.

References

[1] A. Khetani, *Photonic Crystal Fiber as a Biosensor*. Ottawa, ON, Canada: Univ. Ottawa, 2008.
[2] I. Hartl, X. D. Li, C. Chudoba, R. K. Ghanta, T. H. Ko, J. G. Fujimoto, J. K. Ranka, and R. S. Windeler, "Ultrahigh-resolution optical coherence tomography using continuum generation in an air silica microstructure optical fiber," *Opt. Lett.*, vol. 26, no. 9, pp. 608–610, May 2001.
[3] B. Povazay, K. Bizheva, A. Unterhuber, B. Hermann, H. Sattmann, A. F. Fercher, W. Drexler, A. Apolonski, W. J. Wadsworth, J. C. Knight, P. S. J. Russell, M. Vetterlein, and E. Scherzer, "Submicrometer axial resolution optical coherence tomography," *Opt. Lett.*, vol. 27, no. 20, pp. 1800–1802, Oct. 2002.
[4] Y. Wang, Y. Zhao, J. S. Nelson, Z. Chen, and R. S. Windeler, "Ultrahigh-resolution optical coherence tomography by broadband continuum generation from a photonic crystal fiber," *Opt. Lett.*, vol. 28, no. 3, pp. 182–184, Feb. 2003.

[5] Y. Wang, J. Stuart Nelson, Z. Chen, B. J. Reiser, R. S. Chuck, and R. S. Windeler, "Optimal wavelength for ultrahigh-resolution optical coherence tomography," *Opt. Exp.*, vol. 11, no. 12, pp. 1411–1417, Jun. 2003.
[6] G. Humbert, W. Wadsworth, S. Leon-Saval, J. Knight, T. Birks, P. S. J. Russell, M. Lederer, D. Kopf, K. Wiesauer, E. Breuer, and D. Stifter, "Supercontinuum generation system for optical coherence tomography based on tapered photonic crystal fibre," *Opt. Exp.*, vol. 14, no. 4, pp. 1596–1603, Feb. 2006.
[7] T. Schreiber, F. Roser, M. Will, J. Limpert, A. Liem, S. Nolte, and A. Tunnermann, "High repetition rate, high energy fiber CPA system for material processing," in *Proc. IEEE Conf. Lasers Electro-Optics Eur.*, 2005, p. 522.
[8] G. P. Agrawal, *Application of Nonlinear Fiber Optics,* 2nd ed. New York: Academic, 2001.
[9] J. D. Moores, "Nonlinear compression of chirped solitary waves with and without phase modulation," *Opt. Lett.*, vol. 21, no. 8, pp. 555–557, Apr. 1996.
[10] V. I. Kruglov, A. C. Peacock, and J. D. Harvey, "Exact solutions of the generalized nonlinear Schrödinger equation with distributed coefficients," *Phys. Rev. E*, vol. 71, no. 5, pp. 056619-1–056619-11, May 2005.
[11] K. Senthilnathan, Q. Li, K. Nakkeeran, and P. K. A. Wai, "Robust pedestal-free pulse compression in cubic-quintic nonlinear media," *Phys. Rev. A*, vol. 78, no. 3, pp. 033835-1–033835-12, Sep. 2008.
[12] Q. Li, K. Senthilnathan, K. Nakkeeran, and P. K. A. Wai, "Nearly chirp and pedestal-free pulse compression in nonlinear fiber Bragg gratings," *J. Opt. Soc. Amer. B*, vol. 26, no. 3, pp. 432–443, Mar. 2009.
[13] R. V. J. Raja, K. Senthilnathan, K. Porsezian, and K. Nakkeeran, "Efficient pulse compression using tapered photonic crystal fiber at 850 nm," *IEEE J. Quantum Elect.*, vol. 49, no. 12, pp. 1795–1803, Dec. 2010.
[14] A. M. Abobaker, S. Olupitan, S. S. Aphale, K. Nakkeeran, K. Senthilnathan, and P. Ramesh Babu, "Dynamics of 850 nm optical pulses upon compression in a tapered photonic crystal fiber," in *Proc. SIECPC*, 2011, pp. 1–4.
[15] K. Nakkeeran and P. K. A. Wai, "Generalized projection operator method to derive the pulse parameters equations for the nonlinear Schrödinger equation," *Opt. Commun.*, vol. 244, pp. 377–382, 2005.
[16] J. Hu, B. S. Marks, C. R. Menyuk, J. Kim, T. F. Carruthers, B. M. Wright, T. F. Taunay, and E. J. Friebele, "Pulse compression using a tapered microstructure optical fiber," *Opt. Exp.*, vol. 14, no. 9, pp. 4026–4036, May 2006.
[17] J. C. Travers, J. M. Stone, A. B. Rulkov, B. A. Cumberland, A. K. George, S. V. Popov, J. C. Knight, and J. R. Taylor, "Optical pulse compression in dispersion decreasing photonic crystal fiber," *Opt. Exp.*, vol. 15, no. 20, pp. 13203–13211, Oct. 2007.
[18] G. Bouwmans, F. Luan, J. C. Knight, P. S. J. Russell, L. Farr, B. J. Mangan, and H. Sabert, "Properties of a hollow-core photonic bandgap fiber at 850 nm wavelength," *Opt. Exp.*, vol. 11, no. 14, pp. 1613–1620, Jul. 2003.
[19] P. V. Mamyshev, S. V. Chernikov, and E. M. Dianov, "Generation of fundamental soliton trains for high bit-Rate optical fiber communication lines," *IEEE J. Quantum Electron.*, vol. 21, no. 10, pp. 2347–2355, Oct. 1991.
[20] N. M. Litchinister, G. P. Agrawal, B. J. Eggleton, and G. Lenz, "High-repetition-rate-soliton-train generation using fiber Bragg gratings," *Opt. Exp.*, vol. 3, no. 11, pp. 411–417, Nov. 1998.
[21] P. T. Dinda, A. B. Moubissi, and K. Nakkeeran, "Collective variable theory for optical solitons in fibers," *Phys. Rev. E., Stat. Nonlin. Soft Matter Phys.*, vol. 64, no. 1, p. 016608, Jul. 2001.
[22] K. Nakkeeran, Y. H. C. Kwan, P. K. A. Wai, A. Laburyere, P. Tchofo Dinda, and A. B. Moubissi, "Analytical design of densely dispersion-managed optical fiber transmission systems using Gaussian and raised cosine RZ ansatze," *J. Opt. Soc. Amer. B*, vol. 21, no. 11, pp. 1901–1907, Nov. 2004.
[23] H. Zhang, S. Chang, J. Yuan, and D. Huang, *Supercontinuum Generation in Chloroform-Filled Photonic Crystal Fibers*, vol. 121, no. 9, pp. 783–787, May 2010.
[24] S. Yiou, P. Delaye, A. Rouvie, J. Chinaud, R. Frey, G. Roosen, P. Viale, S. Février, P. Roy, J.-L. Auguste, and J.-M. Blondy, "Stimulated Raman scattering in an ethanol core microstructured optical fiber," *Opt. Exp.*, vol. 13, no. 12, pp. 4786–4791, Jun. 2005.